Journal of the European Ceramic Society 39 (2019) 165–172

Contents lists available at ScienceDirect

Journal of the European Ceramic Society

journal homepage: www.elsevier.com/locate/jeurceramsoc

Original Article

Formation and migration of point defects in tungsten carbide: Unveiling the sluggish bulk self-diffusivity of WC

P.A. Burr[a,*], S.X. Oliver[b]

[a] School of Mechanical and Manufacturing Engineering, UNSW Sydney, 2052, NSW, Australia
[b] Graduate School of Biomedical Engineering, UNSW Sydney, 2052, NSW, Australia

ARTICLE INFO

Keywords:
Diffusion
DFT simulations
Tungsten carbide
WC
Defect chemistry

ABSTRACT

The formation and migration of point defects in α-WC was investigated using density functional theory atomic simulations. The material exhibits extremely limited deviation from stoichiometry and only at high temperatures and for carbon deficient conditions (WC_{1-x}). Bulk self-diffusivity was found to be remarkably slow ($\sim 10^{14}$ cm^2/s at 2400 °C) and strongly anisotropic, with basal diffusivity 3–4 orders of magnitude faster than c-axis diffusivity. Our findings help re-interpret previous experimental observations, which were deemed anomalous due to the surprisingly low diffusivity. At equilibrium, the self-diffusivity is dominated by C vacancies, with C interstitials and W defects providing negligible contribution to the total diffusivity. However, under irradiation conditions, interstitial diffusion is predicted to dominate owing to the higher mobility of interstitials once formed ($E_m(C_i) = 1.19$ eV vs $E_m(V_C) = 3.48$ eV). Such diffusion also exhibits strong anisotropy. This may be exploited by means of texture engineering to control the swelling of WC components exposed to radiation fields.

1. Introduction

Tungsten carbide is an extremely hard ceramic with a high melting point (> 3000 K) and excellent thermal and oxidation properties [1,2]. It is commonly used for cutting tools and wear parts in the manufacturing and mining industries [3,4]. Recently it has also been proposed as a radiation shielding material in spherical Tokamak fusion reactors [5] due to the unique combination of light carbon atoms, which slow down neutrons effectively, and heavy tungsten atoms, which provide good attenuation of gamma rays.

Hexagonal α-WC is stable over a wide temperature range, transforming into the cubic rock-salt β-WC at 2755 °C before congruent melting at 2785 °C [6]. The structure of α-WC is hexagonal with lattice parameters $a = 2.90$ Å, $c = 2.85$ Å [7] and alternating layers of W and C (Fig. 1). Notably, unlike many layered hexagonal structures, it exhibits $c/a < 1$, i.e. the nearest neighbour atom of the same species if found out-of-plane instead of in-plane.

When manufacturing the material and when operating in extreme environments of high temperature and/or high radiation fluxes, the diffusion of point defects determines the microstructural evolution of the material, and therefore its macroscopic properties. Carbon self-diffusion has been studied in numerous carbides, including W_2C [8], however only Buhsmer and Crayton [9] have performed diffusivity measurements on WC. Their experiment was a high temperature ^{14}C/WC diffusion couple followed by sub-micron sectioning and auto-radiography. They report two clearly delineated diffusion processes: a fast grain-boundary diffusivity, of similar magnitude to that of other isostructural refractory carbides, and a peculiarly slow bulk diffusivity. The later was deemed to be an anomalous type of bulk diffusion, attributed to some unidentified surface layer effect in the experimental setup.

The diffusivity of a species is the product of species concentration and their mobility. Thus, in this paper, we will first investigate the formation of all intrinsic point defects, validating our results against previous work by Kong et al. [10]. This will also enable an analysis of deviation from stoichiometry and accommodation of disorder. Following that, we build on previous work by calculating the diffusion kinetics of W and C point defects and predicting anisotropic coefficients of self-diffusion. We conclude the paper with a discussion on the effects that radiation damage is predicted to have on the self-diffusivity, and propose mitigation strategies to control such changes.

2. Methodology

2.1. Computational details

All DFT simulations were carried out using the Vienna Ab-Initio Simulation Package (VASP) [11,12] using the PBE formalism of the

* Corresponding author.
E-mail address: p.burr@unsw.edu.au (P.A. Burr).

https://doi.org/10.1016/j.jeurceramsoc.2018.10.001
Received 12 July 2018; Received in revised form 19 September 2018; Accepted 3 October 2018
Available online 06 October 2018
0955-2219/

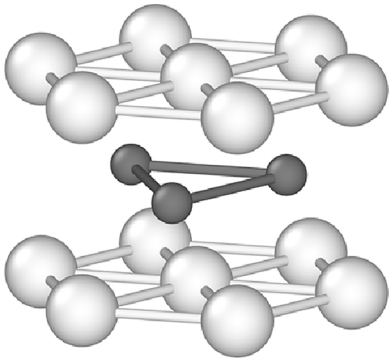

Fig. 1. Hexagonal structure of WC. Small dark spheres represent C atoms, larger white spheres represent W atoms.

generalised gradient approximation for exchange-correlation functional [13] and the undampened D3 Van-der-Waals correction term of Grimme [14,15].

Atoms were described with PAW pseudo-potentials [16] from the VASP5.4 repository with four and fourteen valence electrons for C and W respectively. A consistent plane-wave cut-off of 500 eV was used throughout. k-point sampling of the Brillouin zone was performed with Γ-centered Monkhorst-Pack grids [17] of 12 × 12 × 12 and 3 × 3 × 3 for the unit cell and supercell respectively. Partial occupancies were treated with a first-order Methfessel-Paxton smearing function [18] of width 0.1 eV.

Both unit cell and supercells of the perfect crystal were energy minimised at constant pressure (i.e. internal and external degrees of freedom were relaxed) with symmetry constraints. Defect calculations were then performed in a pre-relaxed 128-atom supercell, consisting of a 4 × 4 × 4 replica of the conventional unit cell, at constant volume (only internal degrees of freedom were minimised) and with no symmetry operations enforced. The convergence criteria for electronic and ionic minimisation was set to 10^{-6} eV and 10^{-5} eV respectively.

Transition states were calculated using climb-image nudged elastic band (c-NEB) simulations [19] with optimised tangent estimates [20], as implemented in the VTST-modified version of VASP [21]. To avoid trapping in metastable states, interstitials and vacancy jumps were simulated with 5 or 7 images, and dumbbell rotations with 3 or 5 images, combined with a force-based LBFGS minimiser, with the convergence criteria set to 0.05 eV/Å.

The formation energy of an intrinsic defect (E_f) is defined according to

$$E_f = E^{DFT}(defect) - E^{DFT}(perfect) \pm n_C E^{DFT}(graphite) \pm n_W E^{DFT}(bcc\text{-}W) \quad (1)$$

where $E^{DFT}(defect)$ and $E^{DFT}(perfect)$ are the DFT total energies of the defective and perfect supercells (of same size), n_C and n_W are null or positive integers representing the number of C and W atoms added to or removed from the supercell to form the defect, respectively. These are then multiplied by the chemical potential of C and W, which is taken from the DFT total energy of the elements in their standard state (graphite/bcc-W).

The use of bcc-W and graphite as the reference states for the chemical potential definition of C and W atoms is consistent with the body of published literature on transition metal carbides [10,22–25], and provides a direct link with experimental standard defect formation energies. However, it is well established that semi-local DFT describes poorly the cohesive energy of graphite, which in turn affects the formation energy of WC defects involving C atoms [24]. To mitigate this source of uncertainty, we used the post-DFT treatment of the Van-der-Waals forces by Grime et al. [15,26], which is known to significantly improve the description of graphite [27], whilst only marginally affecting the structure of dense phases such as W and WC, as shown in Table 1.

2.2. Diffusivity calculations

The diffusivities were calculated within the framework of Onsager transport coefficient (L_{ij}), which links the diffusion flux ($\boldsymbol{J}_i$) to the chemical potentials (μ_i) of species A and B

$$\begin{pmatrix} \boldsymbol{J}_A \\ \boldsymbol{J}_B \end{pmatrix} = -\begin{pmatrix} L_{AA} & L_{AB} \\ L_{BA} & L_{BB} \end{pmatrix} \begin{pmatrix} \nabla\mu_A \\ \nabla\mu_B \end{pmatrix} \quad (2)$$

where L_{ij} are second rank tensors. For tracer diffusion, then there is no correlation between species A and B and the off-diagonal terms L_{AB} and L_{BA} must be zero. In that case, the Onsager matrix is simply a collection of decoupled (Fick's) equations. In the dilute limit the chemical potential of a specie is proportional to its concentration, thus the diffusivity is simply described by

$$D_A = \lim_{c_A \to 0} \frac{k_B T}{c_A} L_{AA} \quad (3)$$

Where a species may diffuse through both interstitial and vacancy-mediated mechanisms, D_A is the sum of the two diffusion mechanisms, each with the respective Onsager coefficient

$$D_A = c_i D_A^i + c_v D_A^v \quad (4)$$

where c_i and c_v are the concentration of A interstitials and vacancies respectively. As we are concerned with self-diffusion, the total sum of $c_i + c_v$ is not fixed to a given concentration, as is the case for solute diffusion [33,34].

Diffusivity calculations were performed within the framework of harmonic transition rate theory. We compute the Onsager matrices using a recently developed Green Function approach [35–37], parameterised by atomic information from the DFT simulations. Accurate description of transport mechanism is underpinned by identifying all likely diffusion networks. For vacancy diffusion, that is straightforward: we considered all symmetry-inequivalent jumps from one lattice-site to the next. For interstitial diffusion, we first identified all stable and metastable sites, and then computed all the jumps between these sites that satisfied the following criteria: 1) the jump did not intersect another stable or metastable state and 2) the jump distance was not greater than one lattice parameter.

Dumbbell configurations were treated as two individual interstitial sites (symmetrically equivalent) connected by a zero-energy jump. As such, there is no distinction between interstitial and interstitialcy

Table 1
Lattice parameters of WC, graphite and tungsten from DFT with and without the D3 correction, and comparison with computational and experimental literature.

	α-WC		C (graphite)		W (bcc)
	a (Å)	*c* (Å)	*a* (Å)	*c* (Å)	*a* (Å)
PBE-D3 (current)	2.910	2.843	2.467	6.931	3.159
PBE (current)	2.925	2.850	2.468	7.582	3.185
PBE	2.932 [10]	2.853 [10]	2.47 [23]	7.72 [23]	3.222 [28]
Experimental	2.889- 2.902 [7]	2.841- 2.849 [7]	2.462 [29,30,31]	6.656-6.707 [29,30,31]	3.165 [28,32]

mechanism, since the two atoms of the dumbbell are indistinguishable. Therefore our calculations yield the self-diffusion constants, not the tracer diffusion constants.

The transition rate between two stable sites, is given by transition rate theory as

$$\omega = \nu \exp\left(-\frac{E_m}{k_B T}\right) \quad (5)$$

where ν is the attempt frequency and E_m is the migration energy, defined as the difference in energy between the transition state and the ground state of the jump.

The prefactors in the Arrhenius equation are known to be of secondary importance compared to the exponential terms [38], and are unlikely to affect results significantly, especially at the high temperature of interest to WC. Nevertheless, we compute the attempt frequency through Vineyard's expression [39].

$$\nu = \frac{\prod_{all} \nu^{GS}}{\prod_{real} \nu^{TS}} \quad (6)$$

where ν^{GS} and ν^{TS} are the vibrational frequencies of the ground state and transition state respectively. The transition state should contain one imaginary frequency, which is ignored. Vibrational frequencies for the full supercell for each state are computationally impracticable and yield high uncertainty due to the large number of frequencies in the product [38]. Therefore, we considered the vibrational frequencies of the hopping atom only, which has shown to yield reasonable results [36,40–42].

3. Results and discussion

3.1. Intrinsic point defects

The formation energy of all intrinsic point defects – vacancies, substitutions and interstitials – have been calculated following equation 1 and shown in Fig. 2. Throughout the text we use the Kröger-Vink notation [43] 'X_S' where X defines the defect species (C, W, and V for carbon atoms, tungsten atoms and a vacancy, respectively), and the subscript $_S$ defines the site (C, W and i for carbon site, tungsten site or interstitial). Only the most stable interstitial of each species is plotted, but various stable interstitials were observed, which are presented in Table 2 along with values reported in the previous DFT study of Kong et al. [10].

Our DFT results are qualitatively in agreement with previous DFT literature, but our calculations systematically yield formation energies

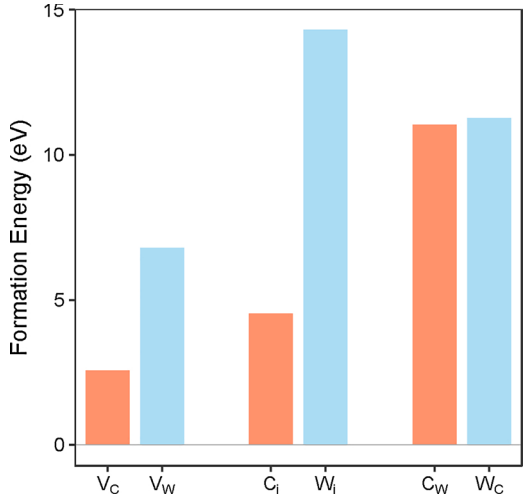

Fig. 2. Formation energy of intrinsic defects, following Kröger-Vink notation [43].

Table 2
Formation energies of vacancies, substitution and interstitial defects. See Fig. 3 for a description of interstitial sites. *c-crowdion (443) relaxed into a kinked variant, where the W atoms are not fully aligned along the [0001] direction (see Fig. 4).

	Formation Energy (eV)	
	Current	Kong et al. [10]
Vacancies		
V_C	2.56	0.39
V_W	6.78	4.14
Substitutions		
C_W	11.03	8.81
W_C	11.27	8.69
C-interstitials		
TriC	4.52	3.41
TriW	7.04	5.00
HexC	7.80	5.63
HexW	6.38	4.37
c-dumbbell	5.83	3.53
a-dumbbell	5.28	3.14
W-interstitials		
TriC	14.31	11.58
TriW	16.37	13.48
HexC	–	–
HexW	19.04	15.96
c-crowdion$^{(443)*}$	16.42	
c-crowdion$^{(444)}$	17.73	13.65
c-crowdion$^{(445)}$	17.18	
c-crowdion$^{(446)}$	16.87	

that are ~1-3 eV larger. The systematic discrepancy could be explained by the unconventional definition of defect formation energy used by Kong et al. [10], see Appendix A for details. Although their definition is internally consistent, it is not possible to make a direct comparison with the current work, or with experimental defect formation energies, without knowing the values of chemical potential of graphite and bcc-W used by Kong et al. [10] (not reported). A further difference with the previous methods is the inclusion of the post-DFT D3 treatment of the Van-der-Waals forces that are important in graphite (see Section 2.1 and Table 1). This correction improves the total energy description of graphite and leads to a systematic increase/decrease of 85 meV for all defects in which a C atom is added/removed.

The formation energy required to accommodate V_C is significantly lower than that of V_W. Similarly, C_i exhibit much lower defect formation energies then W_i, irrespective of lattice site. The lower formation energies of C defects over W defects is consistent with the smaller atomic radius of C (70 pm) compared to W (210 pm) [44]. This suggests that C defects are accommodated much more easily in the WC lattice, and therefore any deviation of stoichiometry is mediated by C defects, either V_C to form WC_{1-x} or C_i to form WC_{1+x}.

Three common stable interstitial sites, TriW, TriC, and HexW were found for W and C atoms (Fig. 3a). In addition, C is stable at the HexC interstitial site and as dumbbells on the basal plane or along the c-axis (Fig. 3b and c), whereas the equivalent defect in W relaxed into a c-crowdion extending over various atomic planes (Fig. 4). Out of these, the TriC site was found to be the most stable for both C and W atoms, having formation energies of 4.52 eV and 14.31 eV respectively.

Given the long-range nature of crowdion defects, these were simulated in various elongated supercells with constant a and b length (11.64 Å or 4 unit cell lengths) and increasing the c axis from 8.52 Å to 17.06 Å, which included 4 × 4 × 3 (96-atoms), 4 × 4 × 4 (128-atoms), 4 × 4 × 5 (160-atoms) and 4 × 4 × 6 (192 atoms) repeating unit cells.

Fig. 4 shows the relaxed configuration of the crowdion and the neighbouring atoms in the four supercell sizes. Increasing the c-axis length results in the crowdion defect extending over a larger number of W atoms, thus reducing the local strain on each atom and resulting in a lower defect formation energy. But despite this, the crowdion defect in

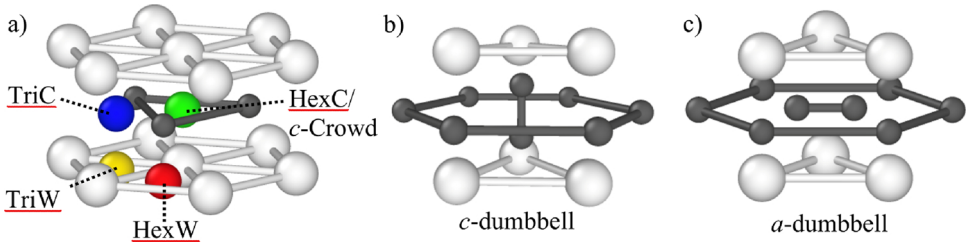

Fig. 3. Stable interstitial sites (a) and carbon dumbbells (b,c). W represented by large light spheres and C by small dark spheres.

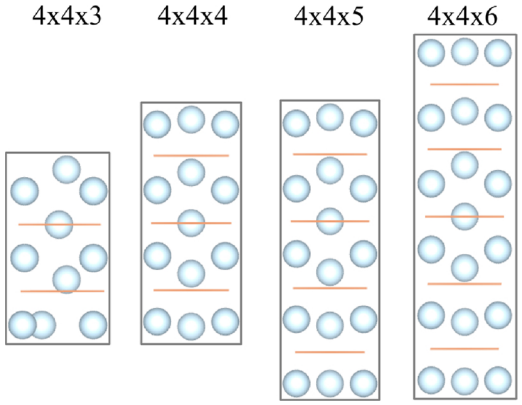

Fig. 4. Final configuration of the W crowdion defect simulated in 4 × 4 × 3, 4 × 4 × 4, 4 × 4 × 5 and 4 × 4 × 6 supercells.

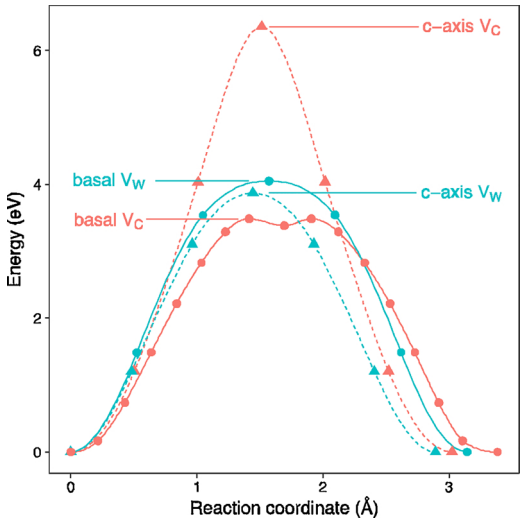

Fig. 5. Minimum energy path of V_C and V_W. Solid and dashed lines represent basal and *c*-axis jumps respectively.

the largest supercell remains considerably less favourable than a W interstitial defect on the TriC site. In the smallest supercell, the crowdion relaxed into a low-symmetry "kinked" elongated defect, where the W atoms were not aligned along the *c*-axis. When simulated in larger supercells, this configuration was not stable, suggesting that it is in fact an artefact due self-interaction across periodic boundary conditions, similarly to what was observed for some defects in metals and ionic compounds [45,46]. Nevertheless, the fact that this kinked configuration exhibits lower energy despite the smaller simulation size suggests that if two crowdions were compressed very close (< 9 Å) then they may rearrange into a more favourable (kinked) configurations, although there is no guarantee that it will be the configuration observed in this particular supercell.

3.2. Diffusion kinetics

For C self-diffusion, both vacancy-mediated and interstitial mechanisms were considered, but for W self-diffusion only the vacancy-mediated process was considered since W_i defects are highly unfavourable and therefore the equilibrium concentration of W_i is expected to be negligible at all relevant temperatures. As the diffusivity is the product of defect concentration and their mobility, the equilibrium diffusivity of W_i is expected to be low irrespective of its mobility (which may be relatively fast due to the formation of extended crowdions as shown in Section 3.1).

For vacancy migration, we considered exchange jumps with the nearest neighbour (of the same species), located either on the same basal plane ([11$\bar{2}$0] jump, or //), or directly above/below ([0002] jump, or ⊥). Fig. 5 shows the activation barrier for migration of V_C and V_W. Tungsten vacancies exhibit near-isotropic behaviour, with migration energies $E_m^{\perp} = 3.87\,eV$ and $E_m^{//} = 4.05\,eV$ respectively, while carbon vacancies exhibit strongly anisotropic behaviour, with enhanced basal migration ($E_m^{//}$= 3.48 eV) and hindered *c*-axis migration ($E_m^{\perp}$= 6.3 eV).

Interstitial carbon diffusion may occur through a number of possible migration pathways described in Fig. 6. The minimum jump network required for carbon interstitial migration comprises a single jump: from the ground state (TriC) to the basal dumbbell (aDB) and back to another TriC site. This jump has a remarkably low migration energy of $E_m = 1.19\,eV$, and enables migration along the basal plane only. A significantly higher energy is required for isotropic diffusion ($E_m = 2.45\,eV$).

Macroscopic transport coefficients were calculated from harmonic transition state theory using an approach based on Green functions [35]. A comprehensive list of all the input parameters for the diffusivity calculations, obtained from DFT, is provided in Appendix B input parameter for Onsager calculation. The resulting diffusion coefficients are plotted against relevant temperature regime in Fig. 7.

As the diffusivity calculations were informed from DFT simulations, any uncertainty surrounding the DFT methodology is propagated here. Of particular concern is the description of graphite using semi-local DFT, which adds uncertainty to the defect formation energy, and therefore to the predicted defect concentration at any given temperature. However, the migration energy is independent of C chemical potential and therefore unaffected by the DFT description of graphite. As such, using a different description of graphite would simply cause a vertical shift in the predicted carbon self-diffusivity curves, whilst the slopes (activation energies) are unaffected.

The present calculations are in excellent agreement with the only experimental measurements of bulk diffusion available in the literature [9], also reported in Fig. 7. Buhsmer and Crayton [9] reported two distinct diffusion mechanism from their measurement of ^{14}C tracer diffusion into a polycrystalline sample: a slower, bulk-like diffusion process in the first 0.5 μm of sample (reproduced in Fig. 7), followed by fast grain-boundary diffusion at deeper penetrations. The initial diffusion, although displaying characteristics of bulk diffusion, was reported as "anomalous surface-layer" diffusion because it was approximately six orders of magnitude slower than expected. But the authors clearly state that the nature of this anomaly is not known. On the other hand, our

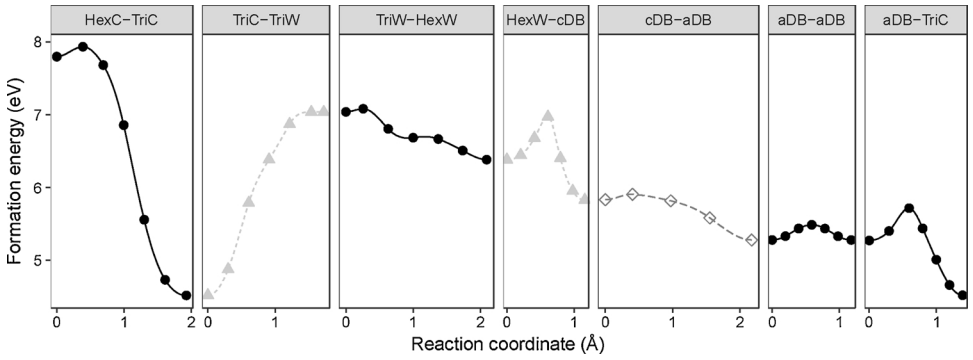

Fig. 6. Minimum energy path for all carbon interstitial jumps. Basal, *c*-axis and prismatic jumps are represented, respectively, by black circles with solid lines, light triangles with dotted lines, and hollow diamonds with dashed lines. Energies are aligned with respect to the most favourable interstitial site, TriC, with formation energy of 4.52 eV.

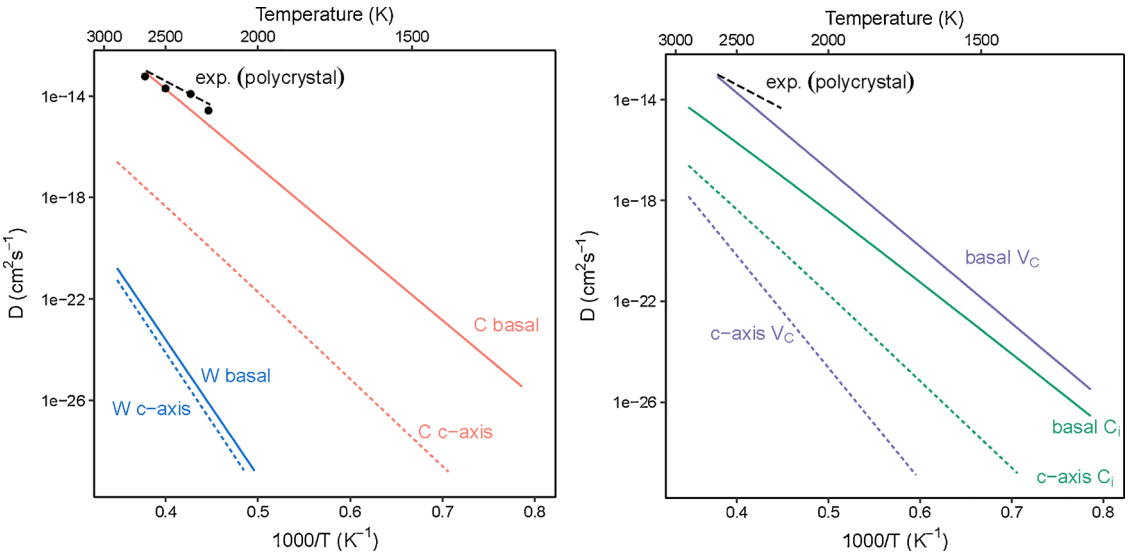

Fig. 7. Left: self-diffusivity of C and W in WC. Experimental values from Buhsmer and Crayton [9]. Right: vacancy-mediated and interstitial components of C self-diffusivity. Basal and *c*-axis diffusion represented with solid and dotted lines respectively.

calculations implicitly represent an idyllic sample with dilute defect, no grain boundary, surface oxidation or other interface effect. The fact that our findings are in excellent agreement with the bulk diffusivity measurement of Buhsmer and Crayton suggests that there is no anomalous surface-layer behaviour, and that the material simply exhibits sluggish bulk diffusion.

The contrast between bulk and gran boundary diffusivity, reported to be ~8 orders of magnitude faster [9], suggests that changing the grain size of a sample would have a large impact on the macroscopic diffusivity, and consequently on the macroscopic properties that arise from it, such as creep, swelling and irradiation growth.

As anticipated, W self-diffusion is practically sessile at all temperatures. On the other hand, the calculated self-diffusivity of C are

$$D_{//} = 0.02 \exp\left(\frac{-577\,kJ}{kT}\right) cm^2 s^{-1}$$

and

$$D_{\perp} = 2.9 \times 10^{-6} \exp\left(\frac{-564\,kJ}{kT}\right) cm^2 s^{-1}$$

for basal ($D_{//}$) and *c*-axis ($D_{\perp}$) respectively.

A strong diffusion anisotropy for C is evident, with basal migration 3–4 orders of magnitude faster than *c*-axis migration. Such strong anisotropy will affect crystal growth during sintering, and may lead to anisotropic creep, swelling and irradiation growth behaviour of WC components exposed to high temperature and/or strong radiation fields. Anisotropic changes in the component in service is clearly undesirable for most applications. This may be mitigated by texture engineering the component during synthesis, such that the basal planes, which are expected to creep/grow most, are aligned in the direction least critical for the specific application.

Carbon self-diffusion appears to be dominated by a vacancy-mediated process, with interstitial jumps contributing less than 0.1% of the overall diffusivity. It is important to note this is due to the lower concentration of interstitials compared to vacancies ($E_f(C_i) = 4.52\,eV$ vs $E_f(V_C) = 2.56\,eV$), not their mobility. In fact, the mobility of the defects once created is significantly higher for interstitials than it is for vacancies ($E_m(C_i) = 1.19\,eV$ vs $E_m(V_C) = 3.48\,eV$). Thus, if defects are created by a non-equilibrium process, such as a collision cascade, the diffusivity of C atoms may increase sharply due to the contribution of out-of-equilibrium population of interstitials. This is relevant to irradiation conditions such as those endured by a plasma-facing material in a Tokamak fusion reactor or spacecraft components. Interestingly, even if the self-diffusion was mediated solely by C interstitials, the anisotropic character of self-diffusion does not vanish, although it is less extreme.

4. Conclusions

The formation and migration of point defects in WC was investigated using density functional theory. The inclusion of a treatment for the Van-der-Waals forces was found to increase the accuracy of defect formation energy (and therefore defect concentration) by improving the description of graphite reference state, and is recommended for all DFT studies of carbides. W defects exhibit significantly higher energy than C defects, and for both species, vacancies are more easily

accommodated then interstitials. The material is predicted to exhibit very limited deviation from stoichiometry, only at high temperatures and for carbon deficiency (WC_{1-x}).

Harmonic transition state theory was used to predict self-diffusion of carbon and tungsten in WC. Bulk self-diffusion was found to be exceptionally sluggish, and in remarkable agreement with high-temperature measurements of Buhsmer and Crayton [9]. This suggests that the experimental observations were not affected by anomalous surface effects as reported in their study, but accurately captured the bulk diffusivity of WC, and that this is significantly slower than expected.

Both interstitial and vacancy-mediated diffusion processes were investigated, with the latter being dominant at all temperatures due to the higher concentration of V_C over C_i. Despite this, carbon self-interstitials exhibit significantly faster mobility than vacancies ($E_m(C_i) = 1.19\,eV$ vs $E_m(V_C) = 3.48\,eV$). Thus, in irradiation conditions, where both vacancies and interstitials defects are produced from collision cascades, the diffusivity of C may increase sharply due to the contribution from self-interstitials.

C self-diffusivity also exhibits a strongly anisotropic behaviour, with basal migration 3–4 orders of magnitude faster than *c*-axis migration. This may be exploited through texture engineering during manufacturing to tailer the macroscopic diffusivity of any WC component. This is particularly relevant for fusion applications, where swelling may be strongly anisotropic given the diffusion anisotropy.

Acknowledgments

PAB acknowledges the Tyree Foundation and the Australian Nuclear Science and Technology Organisation for financial support. This research was undertaken with the assistance of resources and services from the National Computational Infrastructure (NCI), which is supported by the Australian Government, and the Multi-modal Australian ScienceS Imaging and Visualisation Environment (MASSIVE) (www.massive.org.au).

Appendix A. methodology comparison with literature

The current work and that of Kong et al. [10] use very similar methodologies (including the use of the same code), with a few notable exceptions, discussed here. The main difference lies in the definition of defect formation energy and chemical potential, with minor differences also in the details of the computational methodology.

In the current work, we use the conventional definition of defect formation energy (reproduced from Eq. (1)):

$$E_f^{current} = E^{DFT}(defect) - E^{DFT}(perfect) \pm n_C\mu_C \pm n_W\mu_W$$

$$E_f^{current} = E^{DFT}(defect) - E^{DFT}(perfect) \pm n_C E^{DFT}(graphite) \pm n_W E^{DFT}(bcc\text{-}W)$$

where the chemical potential of the WC crystal is taken from a pristine DFT supercell of same size as the defective supercell to maximise cancellation of errors, and the chemical potential of all species added or removed to the supercell is accounted for using the DFT energy of their elemental ground state (graphite and bcc-W).

Kong et al. [10] define the defect formation energy as

$$E_f^{Kong\ et\ al.} = E^{DFT}(defect) - \tfrac{1}{2}(n_W^{'} + n_C^{'})\mu_{WC} - \tfrac{1}{2}(n_W^{'} - n_C^{'})(\mu_W - \mu_C)$$

where $n_W^{'}$ and $n_C^{'}$ are the total number of W and C atoms in the defective supercell (64 for most of their calculations). Their definition can be rewritten in terms of the number of unit cell replicas to form the supercell ($N/2$) and the number of atoms removed to form the defect (n):

$$E_f^{Kong\ etal.} = E^{DFT}(\text{defect}) - (N/2 - n)E^{DFT}(\text{perfect unit cell}) \pm \tfrac{n}{2}(\mu_W - \mu_C)$$

where $N = 64$ in their study and 128 in ours, and $n = 1$ for point defect.

In this form it is clear that the two definitions are not equivalent. Aside for the use of unit cell energy instead of supercell energy for pristine WC (which are in principle identical aside for aliasing error and k-point sampling errors), Kong et al. scale the energy by half the number of atoms of the *defective* cell. In other words, the term "$E^{DFT}(perfect)$" of Eq. (1) is divided by a non-integer number that depends on the supercell size. Another difference lies in the treatment of the chemical potential of the defective atoms: although Kong et al. define μ_W and μ_C from bcc-W and graphite, in line with the current work and previous literature on similar systems [22–25], they use the *difference* in chemical potential "$(\mu_W - \mu_C)$" to define the energy of the defective species.

It must be stressed that their formalism is internally consistent, but it makes direct comparison with the current work, or with experimental defect formation energies, arduous since the value of the chemical potentials are not explicitly provided.

In terms of computational methodology, both studies use the VASP code, PAW pseudopotentials, and GGA exchange-correlation functionals. However, Kong et al use the PW91 formalism, while we employed the PBE formalism, and the pseudopotentials of this study were taken from the revised 5.4 library, which was not available at the time of Kong et al.'s study. These small differences may impart small systematic differences in the results (~ meV), which are a reflection of the state-of-the-art precision of DFT [47].

A final difference between the two study is the addition of a pairwise potential to describe the dispersion force that are important in graphite (the D3 term, which decays with R^{-6}) [15,24,26,27]. This correction improves the total energy description of graphite (see Table 1) from 9.1398 eV for uncorrected DFT to 9.2251 eV for DFT-D3, thereby causing a systematic increase/decrease of 85 meV for all WC defects in which a C atom is added/removed.

Appendix B. input parameter for Onsager calculation

See Table B1.

Table B1
Position, energy and entropy of all transition and ground state of defect used for diffusion analysis. Site entropy for ground states is in unitless, and for transition states it is in THz.

	C Vacancy-mediated	*Site position (unit cell fractional coord.)*	*Relative Energy (eV)*	*Relative site entropy (THz)*
vac	V_C	0.667, 0.333, 0.500	0.0	1.0
jump	$V_C \rightarrow V_C$ (*c*-axis)	0.667, 0.333, 0.500 : 0.667, 0.333, 1.500	6.27	11.516
jump	$V_C \rightarrow V_C$ (basal)	0.667, 0.333, 0.500 :-0.333, 0.333, 0.500	3.48	17.890
	W Vacancy-mediated	*Site position (unit cell fractional coord.)*	*Relative Energy (eV)*	*Relative site entropy (THz)*
vac	V_W	0.000, 0.000, 0.000	0.0	1.0
jump	$V_W \rightarrow V_W$ (*c*-axis)	0.000, 0.000, 0.000 : 0.000, 0.000, 1.000	4.05	6.1383
jump	$V_W \rightarrow V_W$ (basal)	0.000, 0.000, 0.000 : 1.000, 0.000, 0.000	3.87	5.6078
	C interstitial mediated	*Site position (unit cell fractional coord.)*	*Formation Energy (eV)*	*1-atom eigenfrequency (THz)*
i1	i_{TriC}	0.333, 0.667, 0.500	4.522	4940.954
i2	i_{HexC}	0.000, 0.000, 0.500	7.797	12147.314
i3	i_{TriW}	0.333, 0.667, 0.000	7.036	3151.7586
i4	i_{HexW}	0.667, 0.333, 0.000	6.383	14279.619
i5	i_{cDB}	0.667, 0.333, 0.274	5.834	34082.333
i6	i_{aDB}	0.583, 0.070, 0.500	5.280	27980.034
j1	$i_{TriC} \rightarrow i_{HexC}$	0.333, 0.667, 0.500 : 0.000, 1.000, 0.500	7.932	886.116
j2	$i_{TriC} \rightarrow i_{TriW}$	0.333, 0.667, 0.500 : 0.333, 0.667, 0.000	7.036	681.216
j3	$i_{TriW} \rightarrow i_{HexW}$	0.333, 0.667, 0.000 : 0.667, 1.333, 0.000	7.081	586.237
j4	$i_{TriC} \rightarrow i_{aDB}$	0.333, 0.667, 0.500 : 0.487, 0.417, 0.500	5.717	948.928
j5	$i_{HexW} \rightarrow i_{cDB}$	0.667, 0.333, 0.000 : 0.667, 0.333, 0.274	6.971	705.847
j6	$i_{cDB} \rightarrow i_{aDB}$	0.667, 0.333, 0.274 : 0.487, 0.417, 0.500	5.906	1477.232
j7	$i_{aDB} \rightarrow i_{aDB}$	0.583, 0.070, 0.500 : 0.583, 0.513, 0.500	5.488	1191.092
j8	$i_{aDB} \rightarrow i_{aDB}$ (null)	0.583, 0.070, 0.500 : 0.930, 0.417, 0.500	5.280	27980.034
j9	$i_{cDB} \rightarrow i_{cDB}$ (null)	0.667, 0.333, 0.726 : 0.667, 0.333, 1.274	5.834	34082.333

References

[1] S.A. Humphry-Baker, W.E. Lee, Tungsten carbide is more oxidation resistant than tungsten when processed to full density, Scr. Mater. 116 (2016) 67–70.
[2] S.A. Humphry-Baker, K. Peng, W.E. Lee, Oxidation resistant tungsten carbide hardmetals, Int. J. Refract. Met. Hard Mater. 66 (2017) 135–143.
[3] K. Liu, X.P. Li, Ductile cutting of tungsten carbide, J. Mater. Process. Technol. 113 (2001) 348–354.
[4] Z.Z. Fang, X. Wang, T. Ryu, K.S. Hwang, H.Y. Sohn, Synthesis, sintering, and mechanical properties of nanocrystalline cemented tungsten carbide - a review, Int. J. Refract. Met. Hard Mater. 27 (2009) 288–299.
[5] C.G. Windsor, J.M. Marshall, J.G. Morgan, J. Fair, G.D.W. Smith, A. Rajczyk-Wryk, J.M. Tarragó, Design of cemented tungsten carbide and boride-containing shields for a fusion power plant, Nucl. Fusion 58 (2018).
[6] R.V. Sara, Phase equilibria in the system tungsten-carbon, J. Am. Ceram. Soc. 48 (1965) 251–257.
[7] K. Page, J. Li, R. Savinelli, H.N. Szumila, J. Zhang, J.K. Stalick, T. Proffen, S.L. Scott, R. Seshadri, Reciprocal-space and real-space neutron investigation of nanostructured Mo_2C and WC, Solid State Sci. 10 (2008) 1499–1510.
[8] M.R. Andrews, S. Dushman, Diffusion of carbon through tungsten and tungsten carbide, J. Phys. Chem. 29 (1925) 462–472.
[9] C.P. Buhsmer, P.H. Crayton, Carbon self-diffusion in tungsten carbide, J. Mater. Sci. 6 (1971) 981–988.
[10] X.S. Kong, Y.W. You, J.H. Xia, C.S. Liu, Q.F. Fang, G.N. Luo, Q.Y. Huang, First principles study of intrinsic defects in hexagonal tungsten carbide, J. Nucl. Mater. 406 (2010) 323–329.
[11] G. Kresse, J. Furthmüller, Efficiency of ab-initio total energy calculations for metals and semiconductors using a plane-wave basis set, Comput. Mater. Sci. 6 (1996) 15–50.
[12] G. Kresse, J. Furthmüller, Efficient iterative schemes for ab initio total-energy calculations using a plane-wave basis set, Phys. Rev. B 54 (1996) 11169–11186.
[13] J.P. Perdew, K. Burke, M. Ernzerhof, Generalized gradient approximation made simple, Phys. Rev. Lett. 77 (1996) 3865–3868.
[14] S. Grimme, S. Ehrlich, L. Goerigk, Effect of the damping function in dispersion corrected density functional theory, J. Comput. Chem. 32 (2011) 1456–1465.
[15] S. Grimme, J. Antony, S. Ehrlich, H. Krieg, A consistent and accurate ab initio parametrization of density functional dispersion correction (DFT-D) for the 94 elements H-Pu, J. Chem. Phys. 132 (2010) 154104.
[16] G. Kresse, D. Joubert, From ultrasoft pseudopotentials to the projector augmented-wave method, Phys. Rev. B 59 (1999) 1758–1775.
[17] H.J. Monkhorst, J.D. Pack, Special points for Brillouin-zone integrations, Phys. Rev. B 13 (1976) 5188–5192.
[18] M. Methfessel, A. Paxton, High-precision sampling for Brillouin-zone integration in metals, Phys. Rev. B 40 (1989) 3616–3621.
[19] G. Henkelman, B.P. Uberuaga, H. Jonsson, A climbing image nudged elastic band method for finding saddle points and minimum energy paths, J. Chem. Phys. 113 (2000) 9901–9904.
[20] D. Sheppard, R. Terrell, G. Henkelman, Optimization methods for finding minimum energy paths, J. Chem. Phys. 128 (2008) 134106.
[21] Jónsson group & Henkelman group. VTST Tools - http://theory.cm.utexas.edu/vasp/, 2018.
[22] C.R. Weinberger, X.X. Yu, H. Yu, G.B. Thompson, Ab initio investigations of the phase stability in group IVB and VB transition metal nitrides, Comput. Mater. Sci. 138 (2017) 333–345.
[23] X.X. Yu, C.R. Weinberger, G.B. Thompson, Ab initio investigations of the phase stability in tantalum carbides, Acta Mater. 80 (2014) 341–349.
[24] X.X. Yu, G.B. Thompson, C.R. Weinberger, Influence of carbon vacancy formation on the elastic constants and hardening mechanisms in transition metal carbides, J. Eur. Ceram. Soc. 35 (2015) 95–103.
[25] G. Sai Gautam, K.C. Hari Kumar, Elastic, thermochemical and thermophysical properties

of rock salt-type transition metal carbides and nitrides: a first principles study, J. Alloys Compd. 587 (2014) 380–386.
[26] S. Grimme, Semiempirical GGA-type density functional constructed with a long-range dispersion correction, J. Comput. Chem. 27 (2006) 1787–1799.
[27] V. Barone, M. Casarin, D. Forrer, M. Pavone, M. Sambi, A. Vittadini, Role and effective treatment of dispersive forces in materials: polyethylene and graphite crystals as test cases, J. Comput. Chem. 30 (2009) 934–939.
[28] N. Juslin, P. Erhart, P. Träskelin, J. Nord, K.O.E. Henriksson, K. Nordlund, E. Salonen, K. Albe, Analytical interatomic potential for modeling nonequilibrium processes in the W-C-H system, J. Appl. Phys. 98 (2005).
[29] Y.X. Zhao, I.L. Spain, X-ray diffraction data for graphite to 20 GPa, Phys. Rev. B 40 (1989) 993.
[30] A. Ludsteck, Bestimmung der Ånderung der gitterkonstanten und des anisotropen Debye–Waller-Faktors von graphit mittels neutronenbeugung im temperaturbereich von 25 bis 1850°C, Acta Crystallogr. Sect. A A28 (1972) 59–65.
[31] H.J.F. Jansen, A.J. Freeman, Structural and electronic properties of graphite via an all-electron total-energy local-density approach, Phys. Rev. B 35 (1987) 8207.
[32] CRC Handbook of Chemistry and Physics, CRC Press, 2004.
[33] T. Schuler, P. Bellon, D.R. Trinkle, R.S. Averback, Modeling the long-term evolution of dilute solid solutions in the presence of vacancy fluxes, Phys. Rev. Mater. 2 (2018) 073605.
[34] P.A. Burr, M.R. Wenman, B. Gault, M.P. Moody, M. Ivermark, M.J.D. Rushton, M. Preuss, L. Edwards, R.W. Grimes, From solid solution to cluster formation of Fe and Cr in α-Zr, J. Nucl. Mater. 467 (2015) 320–331.
[35] D.R. Trinkle, Automatic numerical evaluation of vacancy-mediated transport for arbitrary crystals: onsager coefficients in the dilute limit using a Green function approach, Philos. Mag. 97 (2017) 2514–2563.
[36] H.H. Wu, D.R. Trinkle, Direct diffusion through interpenetrating networks: oxygen in titanium, Phys. Rev. Lett. 107 (2011) 045504.
[37] R. Agarwal, D.R. Trinkle, Exact model of vacancy-mediated solute transport in magnesium, Phys. Rev. Lett. 118 (2017) 105901.
[38] L. Messina, M. Nastar, N. Sandberg, P. Olsson, Systematic electronic-structure investigation of substitutional impurity diffusion and flux coupling in bcc iron, Phys. Rev. B 93 (2016) 184302.
[39] G.H. Vineyard, Frequency factors and isotope effects in solid state rate processes, J. Phys. Chem. Solids 3 (1957) 121–127.
[40] Jain, A. C. P., Burr, P. A. & Trinkle, D. R. First principles calculations of solute transport in Zirconium I: vacancy mediated diffusion with metastable states, 'in review'.
[41] Jain, A. C. P., Burr, P. A. & Trinkle, D. R. First principles calculations of solute transport in Zirconium II: Interstitial diffusion, 'in review'.
[42] T. Garnier, V.R. Manga, D.R. Trinkle, M. Nastar, P. Bellon, Stress-induced anisotropic diffusion in alloys: complex Si solute flow near a dislocation core in Ni, Phys. Rev. B - Condens. Matter Mater. Phys. 88 (2013) 134108.
[43] F.A. Kröger, H.J. Vink, Relations between the concentrations of imperfections in crystalline solids, Solid State Phys. 3 (1956) 307–435.
[44] J.C. Slater, Atomic radii in crystals, J. Chem. Phys. 41 (1964) 3199–3204.
[45] C. Varvenne, F. Bruneval, M.-C. Marinica, E. Clouet, Point defect modeling in materials: coupling ab initio and elasticity approaches, Phys. Rev. B 88 (2013) 134102.
[46] P.A. Burr, M.W.D. Cooper, Importance of elastic finite-size effects: neutral defects in ionic compounds, Phys. Rev. B 96 (2017) 094107.
[47] K. Lejaeghere, et al., Reproducibility in density functional theory calculations of solids, Science 351 (2016) aad3000.